ACS OMEGA

http://pubs.acs.org/journal/acsodf
Article

Photoelectrochemical Degradation of Diclofenac, Tetracycline, and Amoxicillin in an Aqueous Sulfate Medium: Analysis of Reactive Species

Milda Petruleviciene, Irena Savickaja, Jelena Kovger-Jarosevic, Jurga Juodkazyte, Audrius Padarauskas, Asta Griguceviciene, and Arunas Ramanavicius*

Cite This: *ACS Omega* 2025, 10, 8538−8550

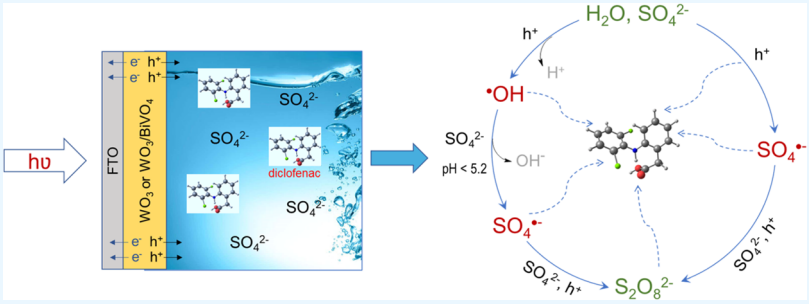

ABSTRACT: As the environment becomes increasingly polluted, there is a pressing need for the development of effective remediation technologies, particularly in the area of wastewater treatment. Recently, there has been growing interest in advanced oxidation systems (AOSs) based on renewable solar energy. This study focuses on the investigation of photoelectrochemical (PEC) AOSs using WO_3 and $WO_3/BiVO_4$ photoanodes and an environmentally friendly aqueous sulfate electrolyte for visible light-induced decomposition of pharmaceutical compounds, namely, diclofenac (DCF), amoxicillin (AMX), and tetracycline (TCC). It was demonstrated that in contrast to conventional persulfate-based advanced oxidation processes, where $S_2O_8^{2-}$ is activated by UV, ultrasound, or thermal energy to generate highly reactive radical species, in photoelectrochemical systems reported here, radicals were generated by the interaction of photogenerated holes with H_2O molecules and SO_4^{2-} ions. These processes eventually led to the formation of $S_2O_8^{2-}$ with an estimated Faradaic efficiency of 70−80%. Persulfate has also been shown to contribute to the degradation of pharmaceutical compounds, particularly diclofenac. The degradation efficiencies of AMX, TCC, and DCF were 10−14, 19−21, and 75−80%, respectively, in both PEC−AOSs studied. The formation of the $WO_3/BiVO_4$ heterojunction enhanced charge carrier separation and stability of the photoanode, but the effect on the pharmaceutical decomposition efficiency was not significant. The mechanism of visible light-induced generation of persulfate in the studied PEC systems was analyzed on the basis of thermodynamic considerations and experimental observations of pH variation during photoelectrolysis.

1. INTRODUCTION

Pharmaceutical compounds detected in aquatic ecosystems have been shown to adversely affect aquatic organisms, raising concerns about the potential contamination of drinking water supplies and highlighting the urgent need to develop innovative technologies to address this issue. Antibiotics, nonsteroidal anti-inflammatory drugs, and other therapeutic agents usually have complex molecular structures that render them resistant to conventional wastewater treatment methodologies.[1−3] Recently, advanced oxidation processes (AOPs), including UV−H_2O_2, Fenton and photo-Fenton, ozone-based technologies, sonolysis, and photocatalysis, have gained significant attention for their effectiveness in degrading pharmaceuticals in aqueous solutions.[4] Among these, persulfate-based AOPs have emerged as a promising alternative to peroxide-based processes due to their enhanced degradation efficiency, which is attributed to the generation of several different reactive radical species upon persulfate activation.[5−8] This can be primarily achieved through thermal, photolytic, sonolytic, and radiolytic treatments as well as through reactions with iron oxide magnetic composites, including in situ-formed iron hydroxides and quinones.[9−11] As a result, AOPs rely on the use of strong oxidants and require significant energy input, prompting the search for more sustainable solutions.

Received: December 1, 2024
Revised: February 5, 2025
Accepted: February 7, 2025
Published: February 17, 2025

Table 1. Comparison of Pharmaceutical Decomposition Efficiencies Reported in the Literature for Photoelectrochemical and Photocatalytic Advanced Oxidation Systems

Material	Pharmaceutical compound	Decomposition efficiency (%)	Electrolyte	Concentration of pharmaceutical compound	Reference
Co_3O_4/WO_3 (photocatalysis)	diclofenac	98.7		15 ppm	37
WO_3/Fe_2O_3	diclofenac	40	H_2SO_4 (pH 2)	10 mg L^{-1}	38
Ag-$BiVO_4$/BiOI	diclofenac	92	0.1 M Na_2SO_4	10 mg L^{-1}	27
ZnO-WO_3 (photocatalysis)	diclofenac	76		10−25 mg L^{-1}	39
N, S−TiO_2/TiO_2 NTs	diclofenac	73.3		5 mg L^{-1}	40
TiO_2 NPs/TiO_2 NTAs	diclofenac	63.6	0.1 M Na_2SO_4	5 mg L^{-1}	41
2D-on-2D WS_2@$CoFe_2O_4$	amoxicillin	99	1 M KOH	10 mg L^{-1}	42
$Ba(Ti_{0.9}Sc_{0.05}Nb_{0.05})O_3$ (BTSN) (photocatalysis)	amoxicillin	92	alkaline (pH 11)	50 mg L^{-1}	43
WO_3 nanoplates	tetracycline	72	0.5 M Na_2SO_4	5 mg L^{-1}	4
g-C_3N_4 nanosheets/TiO_2 nanotube	tetracycline	93	0.1 M Na_2SO_4	10 mg L^{-1}	4
$BiVO_4$/ZnO	tetracycline	66.1	0.1 M Na_2SO_4	20 mg L^{-1}	4
WO_3/Au/FeOOH	tetracycline	98	0.1 M Na_2SO_4 (pH 6.2)	20 mg L^{-1}	34 and 44
$WO_3/BiVO_4$	tetracycline	91	0.1 M Na_2SO_4	10 mg L^{-1}	34 and 35
$WO_3/BiVO_4$ (photocatalysis)	sulfasalazine	65−90		9 mg L^{-1}	30
$WO_3/BiVO_4$	sulfamethoxazole	35−75	NaCl	25 mg L^{-1}	31
$WO_3/BiVO_4$	norfloxacin	70	0.1 M Na_2SO_4	10 mg L^{-1}	32

Photoelectrochemical advanced oxidation systems offer the possibility to harness renewable solar energy to induce oxidative degradation of pharmaceutical contaminants.[12,13] In PEC−AOS, oxidizing species are generated when photo-induced holes in a semiconductor interact with the components of the electrolyte. Therefore, the nature of the semiconductor and the composition of the electrolyte determine which active compounds will be formed.[14,15] Tungsten oxide (WO_3) and bismuth vanadate ($BiVO_4$) are among the most extensively studied photoanode materials, valued for their moderate band gaps of approximately 2.8 and 2.5 eV, respectively, which enable them to absorb a broad spectrum of visible light.[16,17] Moreover, they have deep valence band (VB) positions at 3.2 V and 2.6 vs standard hydrogen electrode (SHE), respectively,[18] thus being able to drive a wide range of oxidation reactions.[19−23] Pure semiconductors, however, face significant challenges related mainly to the significant recombination of photogenerated electrons and holes and susceptibility to photocorrosion. To address these challenges, various approaches have been investigated, such as forming heterojunctions, incorporating metallic nanoparticles and quantum dots, employing cocatalysts, and adding carbon-based materials.[4] Among these strategies, heterojunctions composed of two or more directly interfaced semiconductors have proven highly effective in enhancing photocatalytic performance.[24−26] In a $WO_3/BiVO_4$ heterojunction, charge transfer occurs as a consequence of the alignment of energy levels between the two semiconductors, thereby facilitating the separation of the photogenerated charge carriers. Upon absorbing light, electrons from the valence band (VB) of $BiVO_4$ are promoted to the conduction band (CB), creating holes in the VB. Due to the comparatively lower conduction band position of WO_3, $_4$, electrons in the CB of $BiVO_4$ can readily transfer to the CB of WO_3, whereas holes move from VB of In the field of PEC degradation of pharmaceuticals, various heterostructured photoanodes such as Ag-$BiVO_4$/BiOI, $C_3N_4/BiVO_4$, and 20-Cu/TiO_2 have been tested for the decomposition of diclofenac with reported efficiencies of 68, 68.9, and 71.9%, respectively.[27−29] The $WO_3/BiVO_4$ heterojunction was applied for degradation of sulfasalazine,[30,31] norfloxacin,[32] ibuprofen,[33] tetracycline,[34,35] etc. The results summarized in Table 1 show that the PEC degradation of pharmaceuticals is a promising technique. Although many reported studies have been performed using sulfate as the supporting electrolyte, the degradation of pharmaceuticals is typically attributed to the action of photogenerated hydroxyl radicals.[27−29] However, our previous studies on the PEC activity of WO_3 and $BiVO_4$ photoanodes in an aqueous sulfate medium revealed effective light-assisted formation of persulfate with Faradaic efficiencies (FEs) as high as 80−85%.[14,36]

The objective of this study was to elucidate the impact of in situ-generated persulfate on the degradation of pharmaceutical compounds, specifically diclofenac , amoxicillin, and tetracycline, in PEC−AOSs with WO_3 or $WO_3/BiVO_4$ photoanodes and a simple, environmentally friendly sulfate electrolyte. From the standpoint of applicability, this approach is considerably more straightforward and cost-effective, as it removes the need for costly persulfates and UV illumination. Furthermore, the method allows for the utilization of sulfate ions, which are frequently present in various wastewaters.

Hydrothermal and sol−gel synthesis methods were used to form semiconductor photoelectrodes. Materials were characterized using X-ray diffraction (XRD), scanning electron microscopy (SEM), and energy-dispersive X-ray (EDX) analysis techniques. Photoelectrochemical properties were evaluated using cyclic voltammetry (CV), chronoamperometry (CA), and electrochemical impedance spectroscopy (EIS). The efficiency of light-driven decomposition of DCF, AMX, and TCC was evaluated using UV−vis spectrometry, and the mechanisms of light-induced reactive species formation were analyzed using radical quenching with scavengers. The study demonstrated the significant influence of local pH on the complex interactions occurring during the light-induced formation of reactive radical species. Furthermore, the crucial role of the nature of the semiconductor, which is in direct contact with the electrolyte, on the degradation efficiency was revealed.

https://doi.org/10.1021/acsomega.4c10891
ACS Omega 2025, 10, 8538−8550

2. EXPERIMENTAL SECTION

2.1. Materials. Bismuth (III) nitrate pentahydrate ($Bi(NO_3)_3 \cdot 5H_2O$, 98.0%) from Thermo Fisher Scientific (Waltham, Massachusetts, USA), vanadyl acetylacetonate ($C_{10}H_{14}O_5V$, 99%) from Acros Organics (Geel, Belgium), acetic acid glacial (CH_3COOH, 99.9%) from Reachem (Bratislava, Slovakia), acetylacetone ($C_5H_8O_2$, 99.0%) from Chempur (Piekary Slaskie, Poland), hydrochloric acid (HCl, 35−38%) from Stanlab (Lublin, Poland), sodium sulfate anhydrous (Na_2SO_4, 99.5%) from Chempur (Piekary Slaskie, Poland), methanol (CH_3OH, 99,8%) from Chempur (Piekary Slaskie, Poland), *tert*-butanol ($(CH_3)_3COH$, 99.5%) from Thermo Scientific (Waltham, Massachusetts, USA), sodium tungstate dihydrate ($Na_2WO_4 \cdot 2H_2O$, 99.0%) from Carl Roth (Karlsruhe, Germany), ammonium oxalate monohydrate ($(NH_4)_2C_2O_4 \cdot H_2O$, 99.0%) from Chempur (Piekary Slaskie, Poland), poly(ethylene glycol) (PEG $(C_2H_4O)_nH_2O$) from Carl Roth (Karlsruhe, Germany), diclofenac sodium salt ($C_{14}H_{10}C_{l2}NNaO_2$, ≥98.0%) from Farmalabor (Canosa Di Puglia, Italia), tetracycline hydrochloride ($C_{22}H_{24}N_2O_8 \cdot HCl$, ≥95.0%), amoxicillin ($C_{16}H_{19}N_3O_5S$, 95.0−102.0%) from Sigma-Aldrich (Burlington, Massachusetts, USA), sodium borate decahydrate ($Na_2B_4O_7 \cdot 10H_2O$, ≥95.0%) from Tarchem, Tornowskie Gory, Poland), and boric acid (H_3BO_3, ≥95.0%) from Chempur (Piekary Slaskie, Poland) were used as received from suppliers without further purification.

2.2. Synthesis of WO_3 and $WO_3/BiVO_4$ Coatings. WO_3 coatings on fluorine-doped tin oxide (FTO) substrates were synthesized using the hydrothermal synthesis procedure.[36] First, 0.2593 g of $Na_2WO_4 \cdot 2H_2O$ was dissolved in 30 mL of deionized water. After that, 6 mL of 3 M HCl was added and the solution was stirred for 10 min with a magnetic stirrer at room temperature (∼20 °C). Then, 0.2 g of $(NH_4)_2C_2O_4 \cdot 2H_2O$ and PEG in a molar ratio of W:PEG equal to 1:2 were added to the solution as complexing and structure directing agents, respectively, and the mixture was stirred for 20 min. Next, 34 mL of deionized water were added, and the solution was stirred for 5 min. The resulting mixture was transferred to a stainless steel autoclave. FTO substrates, precleaned in acetone, isopropanol, and water under ultrasonication, were then immersed in the face-down position, and the synthesis was performed at 160 °C for 24 h. Afterwards, the autoclave was left to cool to room temperature. The synthesized coatings were washed 3 times with deionized water and dried in air at 60 °C for 4 h.

A $WO_3/BiVO_4$ heterostructure was formed by depositing a $BiVO_4$ layer on top of a previously synthesized WO_3 coating. $BiVO_4$ sol−gel was prepared by mixing 0.9 mL of 0.2 M $Bi(NO_3)_3 \cdot 5H_2O$ solution in glacial acetic acid and 6 mL of 0.03 M $C_{10}H_{14}O_5V$ solution in acetylacetone. Acetic acid was used for pH control and as a chelating agent, which stabilized Bi in the solution by preventing hydrolysis and precipitation of $Bi(OH)_3$. Acetylacetonate played the role of a chelating agent for the vanadium precursor. The resulting sol−gel was green in color. WO_3-coated FTO slides were immersed into the sol−gel and kept there for 24 h. Finally, the $WO_3/BiVO_4$ coatings were annealed at 400 °C for 2 h in an air atmosphere with a heating ramp of 1 °C min^{-1}. During annealing, the byproducts of the reaction were released in the form of volatile organic compounds and gases (NO_x, CO_2). For some comparative measurements, a $BiVO_4$ coating was deposited directly on the FTO substrate.

2.3. Characterization of the Structure, Surface Morphology, and Chemical Composition of WO_3 and $WO_3/BiVO_4$ Coatings. The crystalline structures of synthesized WO_3 and $WO_3/BiVO_4$ coatings were investigated using an X-ray diffractometer SmartLab (Rigaku) equipped with a 9 kW rotating Cu anode X-ray tube. The analysis covered a 2θ range of 20−80°, utilizing the grazing incidence X-ray diffraction (GIXRD) method with a 0.5° angle (ω) set between the parallel beam of X-rays and the specimen surface. Phase identification was conducted using Match software and the crystallography open database (COD).

WO_3 crystallite size in pure and heterostructured coatings was evaluated according to the following Scherrer equation

$$D = \frac{k\lambda}{\beta \cos \theta} \tag{1}$$

where D is the crystallite size in nm, k is the Scherrer constant equal to 0.9, λ is the X-ray wavelength equal to 0.15406 nm, β is the full width at half-maximum of the diffraction peak (in radians), and θ is Bragg's angle in radians. The three peaks at 2θ positions of 23.6, 24.4, and 34.2° were chosen for the evaluation of D.

The surface morphology and chemical composition of the prepared samples were analyzed using a Helios NanoLab dual beam workstation (Oxford Instruments, the Netherlands) equipped with an energy-dispersive X-ray (EDX) spectrometer at 10 and 20 kV acceleration voltage.

The X-ray photoelectron spectroscopy (XPS) analyses were carried out with a Kratos Axis Supra spectrometer using a monochromatic Al K(α) source (25 mA, 15 kV). The instrument work function was calibrated to give a binding energy (BE) of 83.96 eV for the Au $4f_{7/2}$ line for metallic gold, and the spectrometer dispersion was adjusted to give a BE of 932.62 eV for the Cu $2p_{3/2}$ line of metallic copper. The Kratos charge neutralizer system was used on all specimens. Survey (wide) scan analyses were carried out with an analysis area of 300 μm × 700 μm and a pass energy of 160 eV. High-resolution analyses were carried out with an analysis area of 300 μm × 700 μm and a pass energy of 20 eV. Spectra were charge-corrected to the main line of the carbon 1s spectrum (adventitious carbon) set to 284.8 eV. Spectra were analyzed using CasaXPS software (version 2.3.23rev1.1R).

2.4. Photoelectrochemical Investigations. Cyclic voltammetry, chronoamperometry, and electrochemical impedance spectroscopy measurements were performed using a potentiostat/galvanostat Zennium/Zahner Xpot (Zahner Elektrik, Germany), a three-electrode electrochemical cell, and 0.1 M Na_2SO_4 electrolyte. WO_3 and $WO_3/BiVO_4$ coatings on the FTO substrates were used as working electrodes. A silver/silver chloride electrode with saturated KCl solution ($Ag/AgCl_{(sat.\ KCl)}$) and a Pt plate (1 × 1 cm^2) were used as reference and counter electrodes, respectively. All potential values in the paper are reported vs $Ag/AgCl_{(sat.\ KCl)}$ unless noted otherwise. The electrodes were illuminated from the back side using an light-emitting diode (LED) solar simulator (Redoxme AB, Sweden), which provides illumination approximating natural sunlight (AM1.5G) in the wavelength range of 400−1100 nm with an intensity of 100 ± 2 mW cm^{-2}. EIS measurements were carried out at 0.7 V with an AC voltage amplitude of ±10 mV, within a frequency range from 10^4 to 0.1 Hz under illumination.

Applied bias photon-to-current efficiency (ABPE) measurements were performed in a two-electrode setup with WO_3 or

https://doi.org/10.1021/acsomega.4c10891
ACS Omega 2025, 10, 8538−8550

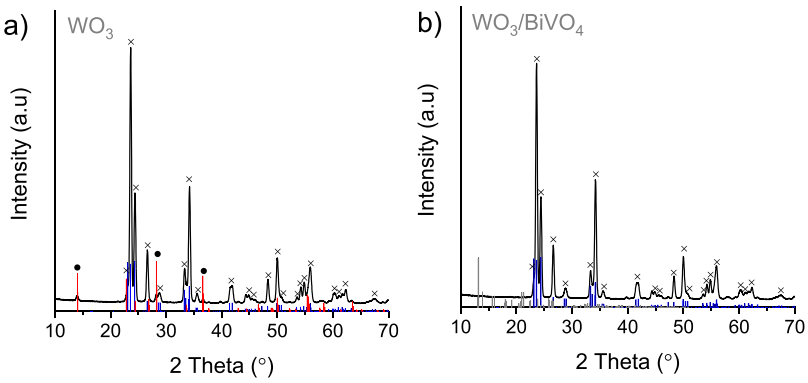

Figure 1. XRD spectra of WO_3 (a) and $WO_3/BiVO_4$ (b) coatings (×—monoclinic WO_3; •—hexagonal WO_3). Blue, red, and gray columns correspond to reference spectra of monoclinic WO_3 (COD: 2106383), hexagonal WO_3 (COD: 1004058), and monoclinic $BiVO_4$ (COD: 9013437), respectively.

$WO_3/BiVO_4$ photoanodes and a Pt wire cathode (Figure S1). The photocurrent was recorded in a solution of 0.1 M Na_2SO_4, with an applied voltage ranging from 0 to 2.5 V (vs Pt) and a potential scan rate of 50 mV s^{-1}. ABPE was calculated according to the following equation:[45,46]

$$\mathrm{ABPE} = \frac{j_{ph}(|V_{redox}| - V_{bias})}{P_{sun}} \times 100\% \quad (2)$$

where j_{ph} is the photocurrent density (mA cm^{-2}), V_{redox} is the thermodynamic potential of a reaction (V), V_{bias} is the applied bias (V), and P_{sun} is the illumination power density (100 mW cm^{-2}). V_{redox} was evaluated, presuming that the photoanodic reaction in Na_2SO_4 electrolyte was oxidation of SO_4^{2-} to $S_2O_8^{2-}$ and the cathodic one was the hydrogen evolution reaction. Given that standard potentials E_a and E_c of the anodic and cathodic half-reactions, respectively, are[36,47]

$$S_2O_8^{2-} + 2e^- \rightarrow 2SO_4^{2-}; \quad E_a^0 = 2.01 \text{ V vs SHE} \quad (3)$$

and

$$2H_2O + 2e^- \rightarrow H_2 + 2OH^-; \quad E_c^0 = 0 - 0.059\,\mathrm{pH} = -0.413 \text{ V vs SHE at pH 7} \quad (4)$$

the thermodynamic potential of the cell reaction is calculated as $V_{redox} = E_c^0 - E_a^0 = -0.413 - 2.01 = -2.423$ V. A negative V_{redox} indicates that the SO_4^{2-} oxidation reaction (eq 5) is not a spontaneous process.

$$2SO_4^{2-} + H_2O \rightarrow S_2O_8^{2-} + H_2 + 2OH^- \quad (5)$$

The formation of reactive sulfate species (RSS) was investigated via photoelectrolysis in a 0.1 M Na_2SO_4 electrolyte in a two-electrode cell at an applied voltage of 1.4 V (vs Pt) until a total charge, Q, of approximately 0.5 C was passed through the system. The electrolyte from the anodic compartment of the cell was then collected and analyzed for the presence of RSS in the form of $S_2O_8^{2-}$ using chromatometric titration. The Faradaic efficiency (FE, %) of the photoelectrochemical generation of persulfate was calculated as the ratio $m_{exp}/m_{theor} \times 100$, where m_{exp} is the experimentally measured mass of $S_2O_8^{2-}$ and m_{theor} is the theoretical mass determined using Faraday's law based on the electric charge passed through the cell during photoelectrolysis. The calculation assumes that the only anodic reaction occurring on the photoanode is the two-electron oxidation of SO_4^{2-} into $S_2O_8^{2-}$. Detailed titration protocols for determining persulfate are reported in our previous studies.[14,48]

Variation of electrolyte pH during photoelectrolysis was measured using a pH meter FiveEasy Plus FP20 (Mettler Toledo, USA).

2.5. Investigation of Decomposition of Pharmaceutical Compounds. Studies on photoelectrochemical decomposition of pharmaceutical compounds were performed in a two-electrode cell with 0.1 M Na_2SO_4 electrolyte containing 50 mg L^{-1} of DCF, AMX, or TCC at an applied voltage of 1.4 V (vs Pt). 0.1, 0.3, 0.5, and 1 C of charge were passed through the cell in separate experiments. A fresh portion of the electrolyte was used each time. After photoelectrolysis, the solution from the anodic compartment of the cell was collected, and the degradation efficiency, η, was evaluated using a UV−vis spectrophotometer Lambda 35UV/VIS (PerkinElmer, USA)

$$\eta = \left(\frac{C_0 - C}{C_0}\right) \times 100\% \quad (6)$$

where C_0 is the initial concentration and C is the remaining concentration of a pharmaceutical.

To compare the decomposition efficiency under different conditions, solutions of DCF, AMX, and TCC were also subjected to photocatalytic, electrochemical, and chemical oxidation treatments. In the latter case, $K_2S_2O_8$ was added to 0.1 M Na_2SO_4 containing 50 mg L^{-1} of DCF, AMX, or TCC. The calculated amounts of the oxidant corresponded to the mass of persulfate that would be formed during photoelectrolysis after passing 0.1, 0.3, 0.5, or 1 C of charge, assuming that the FE of the PEC persulfate generation was 100%. After the addition of the oxidant, the electrolytes were kept for 25 h to provide enough time for the reaction to proceed, and after that, the efficiency of pharmaceutical decomposition was evaluated spectrophotometrically (eq 6). In photocatalytic treatment, no external potential was applied, and the system was illuminated for the same periods of time, which were required in the PEC experiment to pass 0.1, 0.3, 0.5, or 1 C of charge. Similarly, in electrochemical oxidation experiments, electrolysis at 1.4 V (vs Pt) in the dark was performed for the same periods of time. The electrolytes were then collected and subjected to spectrophotometric analysis.

2.6. Studies of the DCF Decomposition Mechanism. The mechanism of photoelectrochemical decomposition of

https://doi.org/10.1021/acsomega.4c10891
ACS Omega 2025, 10, 8538−8550

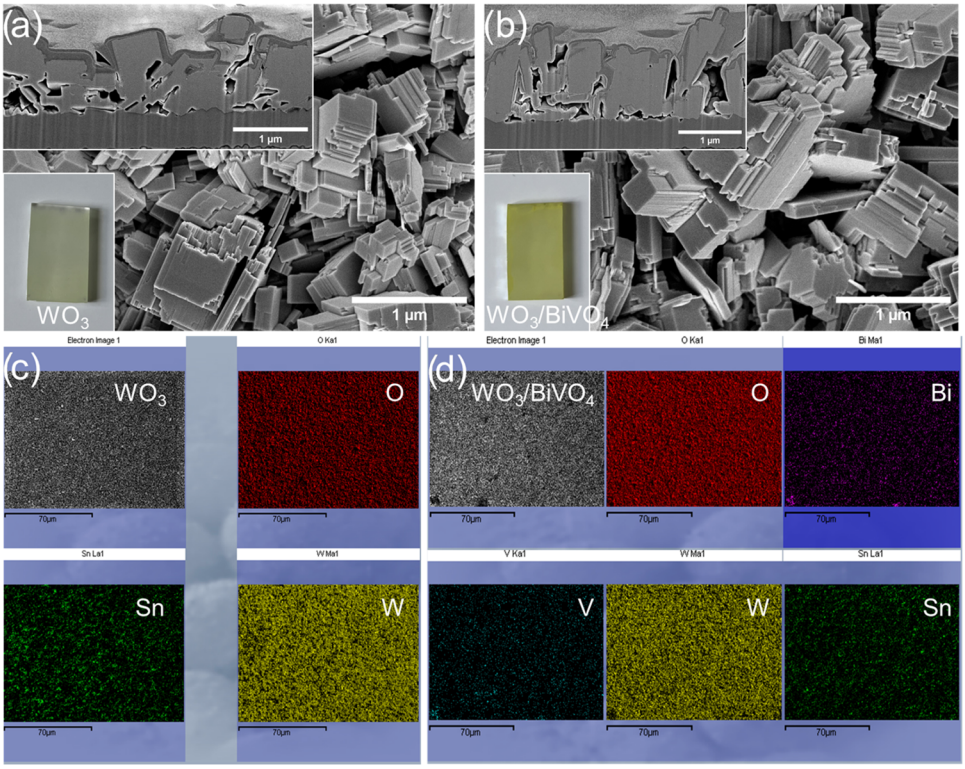

Figure 2. SEM (a, b) and EDX elemental mapping (c, d) images of WO_3 and $WO_3/BiVO_4$ coatings.

DCF was studied using *tert*-butanol (*t*-BuOH), methanol (MeOH), and ammonium oxalate (AO) as scavengers for sulfate radicals, hydroxyl radicals, and photogenerated holes, respectively. Experiments were performed with 0.1 M Na_2SO_4 electrolyte containing 50 mg L^{-1} of DCF and 2 mM of scavenger. Three different electrolytes were prepared for this purpose. The parameters of the PEC−AOS system were the same as those in the photoelectrochemical experiments described above. Samples of the electrolyte for the spectrophotometric evaluation of DCF concentration were sequentially collected from the anodic compartment of the cell after passage of 0.1, 0.3, 0.5, and 1 C of charge.

3. RESULTS AND DISCUSSION

3.1. Structural and Morphological Analysis of the Coatings. X-ray diffraction analysis was conducted to assess the crystalline structure of the synthesized coatings. Peaks corresponding to the monoclinic (COD: No. 2106382) and hexagonal (COD: 1004057) phases can be observed in the XRD spectra of WO_3 (Figure 1a). The diffractogram of the $WO_3/BiVO_4$ sample displays only the peaks of monoclinic WO_3 (Figure 1b). The absence of the hexagonal phase in the latter case can be explained by its transformation into monoclinic during the additional annealing applied in the synthesis of $WO_3/BiVO_4$, since the hexagonal structure is metastable and is usually formed at lower annealing temperatures.[49] This additional annealing, however, did not affect the WO_3 crystallite size, which was found to be 25.3 nm for both WO_3 and $WO_3/BiVO_4$. Peaks attributable to the $BiVO_4$ crystalline phase are absent in the diffractograms of the $WO_3/BiVO_4$ heterostructure (Figure 1b), indicating that the bismuth vanadate layer is extremely thin (Figure S2).

The surface morphologies of the layers were also found to be very similar. The coatings consisted of large cubic WO_3 crystals, up to one micron in size, with stepped edges (Figure 2a,b). Although $BiVO_4$ is scarcely discernible in SEM images, the lower insets in Figure 2a,b clearly demonstrate the different colors of WO_3 and $WO_3/BiVO_4$ samples. To confirm the deposition of $BiVO_4$, energy-dispersive X-ray spectroscopy and X-ray photoelectron spectroscopy analyses were performed. The EDX results presented in Table 2 and Figure S2, in conjunction with the elemental mapping images in Figure 2c,d, demonstrate the presence of Bi and V elements in the heterostructured sample. The chemical states of the elements were subsequently verified through XPS.

Table 2. EDX Analysis Results for the WO_3 and $WO_3/BiVO_4$ Samples

Sample	Element (atom %)				
	O	W	Sn	V	Bi
WO_3	71.25	80.33	1.98		
$WO_3/BiVO_4$	70.02	26.76	2.03	0.72	0.48

High-resolution spectra of both WO_3 and $WO_3/BiVO_4$ (Figure S3a−d) exhibit peaks at 35.7 and 37.85 eV corresponding to the W $4f_{7/2}$ and W $4f_{5/2}$ electrons in the W^{6+} oxidation state, whereas the peak at 530.4 eV is attributed to the O 1s electron in O^{2-}.[33,50] Peaks at 159.5 and 169.8 eV in the spectrum of the heterostructured sample are assigned to Bi $4f_{7/2}$ and Bi $4f_{5/2}$ electrons in Bi^{3+}, respectively (Figure S3e), and peaks at 517 and 524 eV correspond to V $2p_{3/2}$ and V $2p_{1/2}$ electrons of V^{5+}, respectively (Figure S3f).[50−52] Small features attributable to V^{4+} can be seen in the lower binding energy range (Figure S3f). The Bi/V ratio was found to be ∼1:1, while the presence of W peaks in the spectra of the $WO_3/BiVO_4$ surface suggests that the $BiVO_4$ layer may not form continuous coverage over the WO_3 surface.

https://doi.org/10.1021/acsomega.4c10891
ACS Omega 2025, 10, 8538−8550

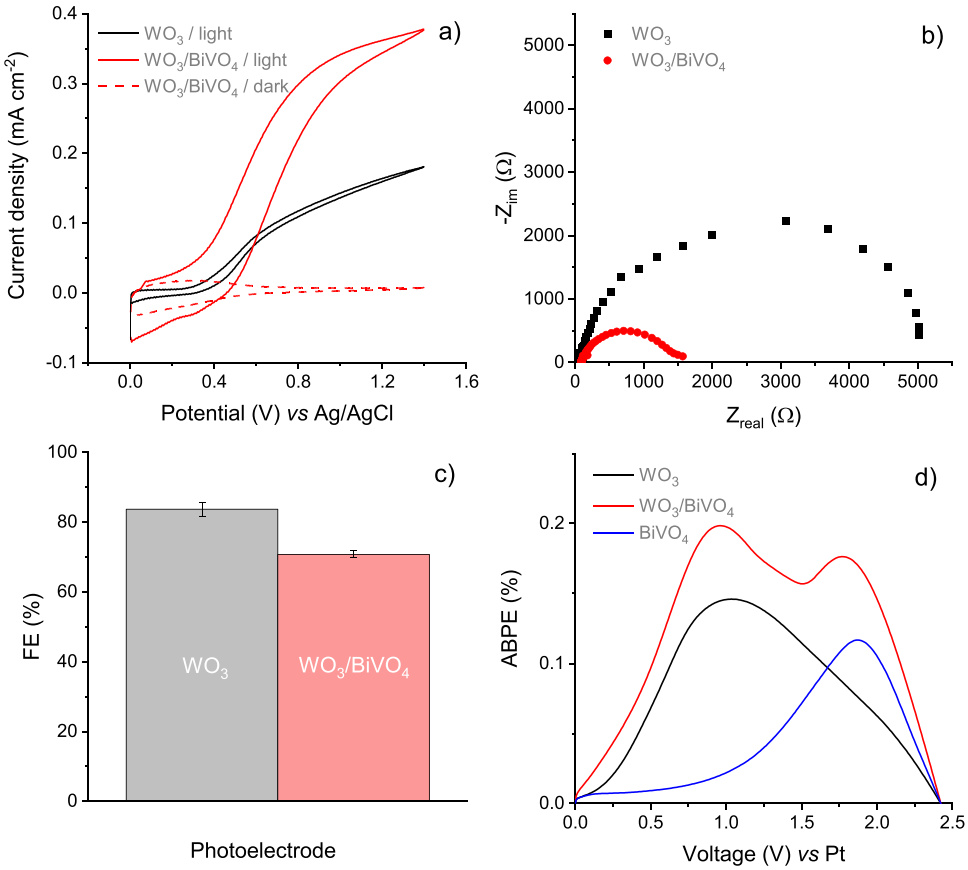

Figure 3. Characterization of the photoelectrochemical activity of WO_3 and $WO_3/BiVO_4$ coatings in 0.1 M Na_2SO_4 electrolyte: (a) cyclic voltammograms recorded at 50 mV s^{-1} scan rate, (b) Nyquist plots recorded at 0.7 V, (c) Faradaic efficiencies of PEC generation of persulfate, and (d) applied bias photon-to-current efficiencies of WO_3, $BiVO_4$, and $WO_3/BiVO_4$ photoelectrodes.

3.2. Photoelectrochemical Analysis. The cyclic voltammetry was employed for the preliminary assessment of the PEC activity of the synthesized WO_3 and $WO_3/BiVO_4$ coatings in 0.1 M Na_2SO_4 electrolyte (Figure 3a). In the absence of illumination, the current was negligible, whereas under illumination, the maximum photocurrents, j_{ph}, generated by WO_3 and $WO_3/BiVO_4$ were 0.18 and 0.38 mA cm^{-2}, respectively. The fact that the photocurrent of the $WO_3/BiVO_4$photoelectrode was almost twice as high as that of WO_3 and the onset of j_{ph} was observed at lower potentials, clearly indicates that the formation of a heterojunction significantly facilitates the separation and transfer of photogenerated charge carriers. This was corroborated by electrochemical impedance spectroscopy measurements, which showed that charge transfer resistance, R_{ct}, proportional to the diameter of the semicircle in the Nyquist plot, was more than 3 times larger for WO_3 electrodes compared to $WO_3/BiVO_4$ (Figure 3b). The imaginary impedance, which corresponds to the electrochemical capacitance of the coating, was higher for the $WO_3/BiVO_4$ heterojunction compared to the pure WO_3 coating.

The analysis of the products of photoanodic processes occurring on the surface of WO_3 and $WO_3/BiVO_4$ electrodes in 0.1 M Na_2SO_4 revealed the predominant formation of reactive sulfate species. The FE of PEC generation of $S_2O_8^{2-}$ on WO_3 was approximately 82%, whereas for $WO_3/BiVO_4$, it was around 70% (Figure 3c). The slight decrease in FE due to the deposition of the $BiVO_4$ layer on WO_3 is most likely an indication of a more significant contribution of the competing light-induced oxygen evolution reaction (OER), which is the most probable competing photoanodic process in the studied system.[4,8,53] A sample of pure $BiVO_4$ on FTO was also prepared and tested for comparison. However, the photocurrent of a thin $BiVO_4$ layer was found to be very low, measuring several microamperes. Furthermore, no photoelectrochemically generated persulfate was found by the titrimetric analysis of the electrolyte after more than 2 h of photoelectrolysis or the amount of $S_2O_8^{2-}$ was below the detection limit of the analytical method used. Further analysis was conducted to evaluate the applied bias photon-to-current efficiency of reaction 5 in the studied system. As shown in Figure 3d, the ABPE plot of the $WO_3/BiVO_4$ sample revealed the presence of two peaks at positions corresponding to those of the pure WO_3 and $BiVO_4$ materials. However, the values of ABPE for the heterostructure were higher, suggesting the enhancement of electronic properties in the composite. A similar phenomenon was reported in ref 54, where double peaks in incident photon-to-current efficiency (IPCE) plots were observed for the $WO_3/BiVO_4$ heterojunction.

3.3. Study of Light-Induced Decomposition of Diclofenac, Tetracycline, and Amoxicillin in an Aqueous Sulfate Medium. WO_3 and $WO_3/BiVO_4$ samples were further used in the studies of light-assisted degradation of biologically active compounds in an aqueous sulfate medium. A solution of 0.1 M Na_2SO_4 containing 50 mg L^{-1} of diclofenac, amoxicillin, or tetracycline was subjected to photoelectrolysis, as described in the Section 2. Decomposition efficiencies as a function of charge consumed in photo-

https://doi.org/10.1021/acsomega.4c10891
ACS Omega 2025, 10, 8538−8550

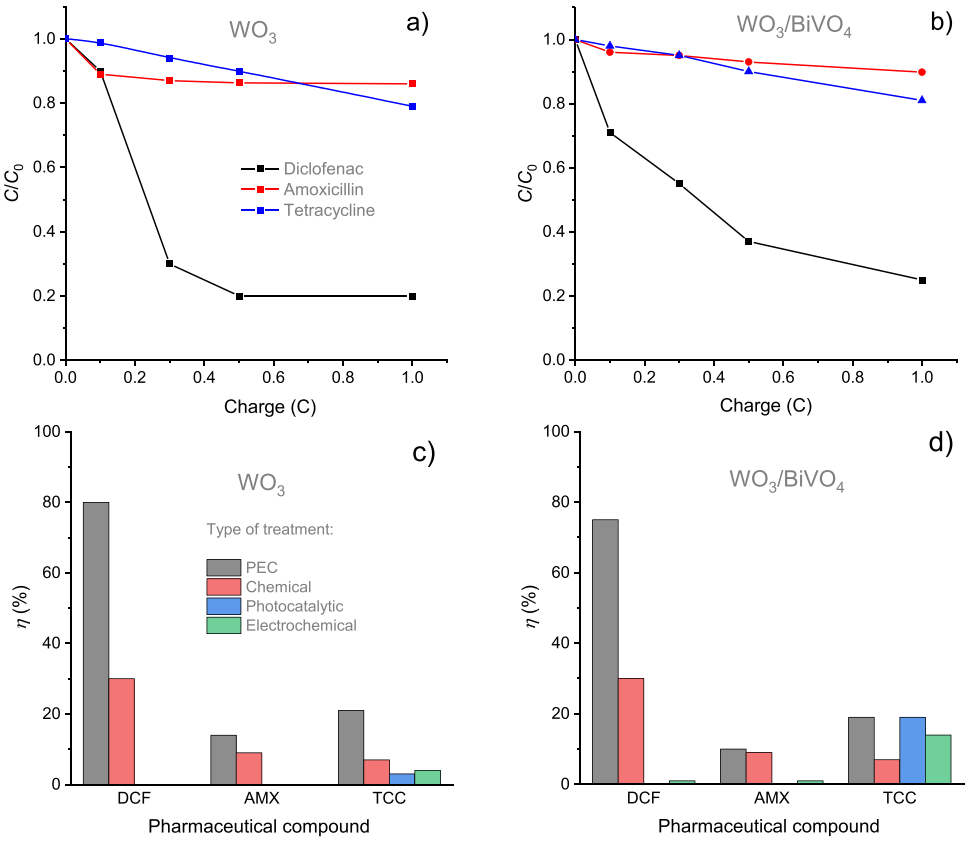

Figure 4. Progression of pharmaceutical compound degradation depicted by the normalized concentration ratio (C/C_0) as a function of charge consumed during photoelectrolysis of 0.1 M Na_2SO_4 solution containing 50 mg L^{-1} of DCF, AMX, or TCC using (a) WO_3 or (b) $WO_3/BiVO_4$ photoelectrode. Comparison of pharmaceutical compound degradation efficiency under different oxidative treatments including chemical with $S_2O_8^{2-}$, photoelectrochemical, electrochemical, and photocatalytic treatments in AOS systems with (c) WO_3 and (d) $WO_3/BiVO_4$ (see the Section 2 for the detailed description of conditions applied in these experiments).

electrolysis are compared in Figure 4. It is worth noting that the normalized concentration ratio (C/C_0) is typically plotted against time rather than the charge. However, due to fluctuations in photocurrent, plotting it against charge was deemed more appropriate and accurate. The degradation of DCF was clearly the most effective among the pharmaceutical compounds studied and occurred significantly faster on WO_3 than on $WO_3/BiVO_4$. For WO_3, approximately 80% (±5%) decomposition was achieved after the passage of just 0.5 C, whereas for $WO_3/BiVO_4$, a charge of 1 C was required to achieve a similar level of DCF decomposition. The PEC degradation of AMX and TCC occurred at a markedly slower rate and with a significantly lower efficiency for both photoelectrodes. Further experiments were conducted to observe the progression of pharmaceutical degradation over time in electrolytes that underwent PEC treatment. For this purpose, the collected samples were subjected to repeated UV−vis spectroscopic analysis after a period of 48 h. Figure S4 illustrates that in the case of DCF, almost complete decomposition (η = 96 ± 5%) was achieved with both photoanodes, whereas for AMX and TCC, the degradation progress was slight to negligible.

These findings illustrate that despite the enhanced charge separation in the $WO_3/BiVO_4$ heterojunction, the decomposition efficiency of the studied compounds is strongly influenced by the intrinsic properties of the semiconductor, which is in direct contact with the electrolyte, as well as the chemical composition of pharmaceuticals themselves.[34,55,56] Therefore, it is important to optimize the PEC−AOSs to achieve complete decomposition of studied antibiotics.[34,57,58]

The efficiency of pharmaceutical degradation in the PEC−AOS system was compared with the results obtained when these compounds were subjected to either electrochemical, photocatalytic, or chemical oxidative treatments. In the latter case, the calculated amount of $S_2O_8^{2-}$, corresponding to Q of 0.1, 0.3, 0.5, or 1 C and assuming the Faradaic efficiency of SO_4^{2-} oxidation to $S_2O_8^{2-}$ of 100%, was added to 0.1 M Na_2SO_4 electrolyte containing 50 mg L^{-1} of DCF, TCC, or AMX. The photoelectrochemical treatment demonstrated superior efficiency in the decomposition of DCF when compared to all other treatments involving both photoelectrodes (Figures 4c,d and S4). The average η for DCF was ∼80%, whereas for AMX, it ranged between 10 and 14% and remained at approximately 20% for TCC. Another obvious fact is that photocatalytic and electrochemical treatments were absolutely ineffective in the degradation of DCF and AMX for both WO_3 and $WO_3/BiVO_4$. In the case of TCC, different results were obtained with the $WO_3/BiVO_4$ heterojunction, where degradation efficiencies of 20 and 17% were achieved for photocatalytic and electrochemical treatments, respectively (Figure 4d). The chemical treatment with $S_2O_8^{2-}$ was found to be more efficient for the degradation of DCF than that of the other two compounds. However, η was only 30%, which is almost three times lower than that of the PEC treatment with any of the photoelectrodes. The chemical action of the photoelectrochemically generated $S_2O_8^{2-}$ (Figure 3c) can

https://doi.org/10.1021/acsomega.4c10891
ACS Omega 2025, 10, 8538−8550

explain the progression of DCF degradation over the 48 h period after the PEC treatment described above (Figure S4). Nevertheless, these findings suggest that in addition to $S_2O_8^{2-}$, some other reactive species may also be involved in the degradation of the assessed pharmaceuticals. Given that the PEC degradation of diclofenac was the most facile, further studies were conducted to gain deeper insights into the mechanism of light-assisted decomposition of this compound and the nature of the reactive species.

3.4. Investigation of the Diclofenac Decomposition Mechanism. Radical species that may be generated by the interaction of photoinduced holes with the components of the Na_2SO_4 electrolyte are as follows[47]

$$SO_4^{2-} + h^+ \rightarrow SO_4^{-\bullet}; \quad E^0 = 2.437 \text{ V vs SHE} \tag{7}$$

$$H_2O + h^+ \rightarrow HO^\bullet + H^+; \quad E^0 = (2.730 - 0.059\text{pH}) \text{ V vs SHE} \tag{8}$$

It is noteworthy that the potential of hydroxyl radical formation (eq 8) as well as the potentials of conduction and valence band (CB and VB) of metal oxide semiconductors are pH dependent and shift negatively by 0.059 pH with increasing pH.[59,60] Considering that the VB positions in WO_3 and $BiVO_4$ at pH = 0 are ∼3.2 eV[60] and ∼2.9 V,[59] respectively, it can be inferred that photogenerated holes would be sufficiently energetic to oxidize electrolyte species to highly reactive $HO^\bullet$ and $SO_4^{-\bullet}$ radicals. The formation of these radicals has been evidenced in numerous studies using such techniques as electron paramagnetic resonance, transient absorption spectroscopy, quenching, etc.[8,53,54] The latter approach was applied in this study to investigate the mechanism of the photoelectrochemical degradation of DFC with WO_3 and WO_3/$BiVO_4$ photoanodes.

Ammonium oxalate (AO), *tert*-butyl alcohol (TBA), or methanol (MeOH) was added to 0.1 M Na_2SO_4 + 50 mg L^{-1} DCF electrolyte as h^+ or radical ($HO^\bullet$, $SO_4^{-\bullet}$) scavengers[61−63] and PEC degradation of DCF was monitored as previously described. According to the literature, TBA is used as the $HO^\bullet$ scavenger,[63,64] and MeOH as the $SO_4^{-\bullet}$ scavenger;[63] however, in fact, both alcohols scavenge both radicals, but at significantly different rates.[65] As shown in Table 3, the reaction of MeOH with $HO^\bullet$ is about 300 times faster than that with $SO_4^{-\bullet}$, while in the case of TBA, this difference is even larger, i.e., from 400 to 1900. Another important aspect is that MeOH reacts faster with both radicals compared to TBA.

Table 3. Radical Scavenging Reaction Rate Constants[a]

Scavenger	Reaction rate constant (M^{-1} s^{-1})	
	$SO_4^{-\bullet}$	$HO^\bullet$
MeOH	3.2×10^6	9.7×10^8
TBA	$(4–9.1) \times 10^5$	$(3.8–7.6) \times 10^8$

[a]Adapted with permission from ref 65. Copyright 2009 American Chemical Society.

The results presented in Figure 5a,b demonstrate that the quenching of holes with OA had the most pronounced effect in suppressing the degradation of DFC for both photoanodes. However, the efficacy of AO diminished over time, likely due to the consumption of this scavenger during longer experiments. In the case of WO_3 (Figure 5a), the addition of TBA or MeOH had almost the same effect on the DFC degradation rate, with more than 50% of DCF remaining undecomposed when a charge equal to 1 C was passed through the electrochemical cell. Considering the significant influence of electrolyte pH on the arrangement of energetic levels of $HO^\bullet$ and $SO_4^{-\bullet}$ formation, variation of 0.1 M Na_2SO_4 solution pH during photoelectrolysis with both photoelectrodes was evaluated in a separate experiment (Figure 5c). After the passage of 1 C of charge, the pH of the electrolyte decreased from an initial value of 5.6 to 4.2 . Slightly acidic initial pH of 0.1 M Na_2SO_4 solution can be explained by the absorption of CO_2 from the air. In order to understand how the changes in the electrolyte pH affect the arrangement of energy levels of the reactant species, specifically the holes in the VB of WO_3 and $BiVO_4$, with respect to the potentials of $HO^\bullet/H_2O$ and $SO_4^{-\bullet}/SO_4^{2-}$, the E−pH diagram was plotted and is shown in Figure 5d. It can be seen that at a pH of ∼5.2, the potentials of the reactions 7 and 8 become practically equal. Consequently, at pH > 5.2, the formation of $HO^\bullet$ is thermodynamically favored, whereas at pH < 5.2, the formation of $SO_4^{-\bullet}$ becomes more favorable. Another important aspect to consider is that at pH < 5.2, $HO^\bullet$ can oxidize SO_4^{2-} to $SO_4^{-\bullet}$, whereas at pH > 5.2, $SO_4^{-\bullet}$ can oxidize H_2O to $HO^\bullet$. The working pH range (Figure 5c) is just around 5.2, which means that the potentials of $HO^\bullet$ and $SO_4^{-\bullet}$ formation are rather close in both photoelectrochemical systems studied. The decrease in pH was a little faster in the case of the WO_3 photoelectrode, implying that the probability of $SO_4^{-\bullet}$ formation was increasing faster. This is in agreement with slightly higher FEs of $S_2O_8^{2-}$ formation observed for the WO_3 photoelectrode (Figure 3c). In the case of the WO_3/$BiVO_4$ photoelectrode, the influence of the scavengers on the degradation of DCF was different: the presence of TBA suppressed the degradation rate of diclofenac more significantly than the addition of MeOH (Figure 5b). Although the effects of both scavengers were almost equal up to Q = 0.1 C, the influence of MeOH was inferior at longer photoelectrolysis times. It is difficult to explain this phenomenon, especially since the quenching of $HO^\bullet$ with TBA had a very strong effect on DCF degradation, and MeOH should quench these radicals even faster. Such a result could be related to the nature of the semiconductor at the surface of the composite film, i.e., $BiVO_4$, and/or some (photo)chemical interactions between the species present in this particular photoelectrochemical system.

In general, it is challenging to determine the dominant role of a particular radical in the photoelectrochemical systems under investigation due to the proximity of the $HO^\bullet/H_2O$ and $SO_4^{-\bullet}/SO_4^{2-}$ potentials within the working pH range (Figure 5c,d). Local variations in the pH at the photoelectrode surface can render these chemical equilibria highly dynamic. The mechanisms of radical and nonradical formation of persulfate in the photoelectrochemical systems investigated are schematically summarized in Figure 6. The higher efficiency of photoelectrochemical degradation of diclofenac found for WO_3 could be attributed to the higher oxidizing power of VB holes, which have a larger energy offset to drive the oxidation of solution species.

3.5. Photoelectrode Stability Tests. WO_3 and WO_3/$BiVO_4$ photoelectrodes were subjected to prolonged photoelectrolysis in 0.1 M Na_2SO_4 electrolyte containing 50 mg L^{-1} of DCF. The results of cumulative 14 h-long stability tests are presented in Figure S6. After each electrolysis session, the electrolyte was replaced with a fresh one. The results reveal satisfactory stability of photocurrent: stationary values reached

https://doi.org/10.1021/acsomega.4c10891
ACS Omega 2025, 10, 8538−8550

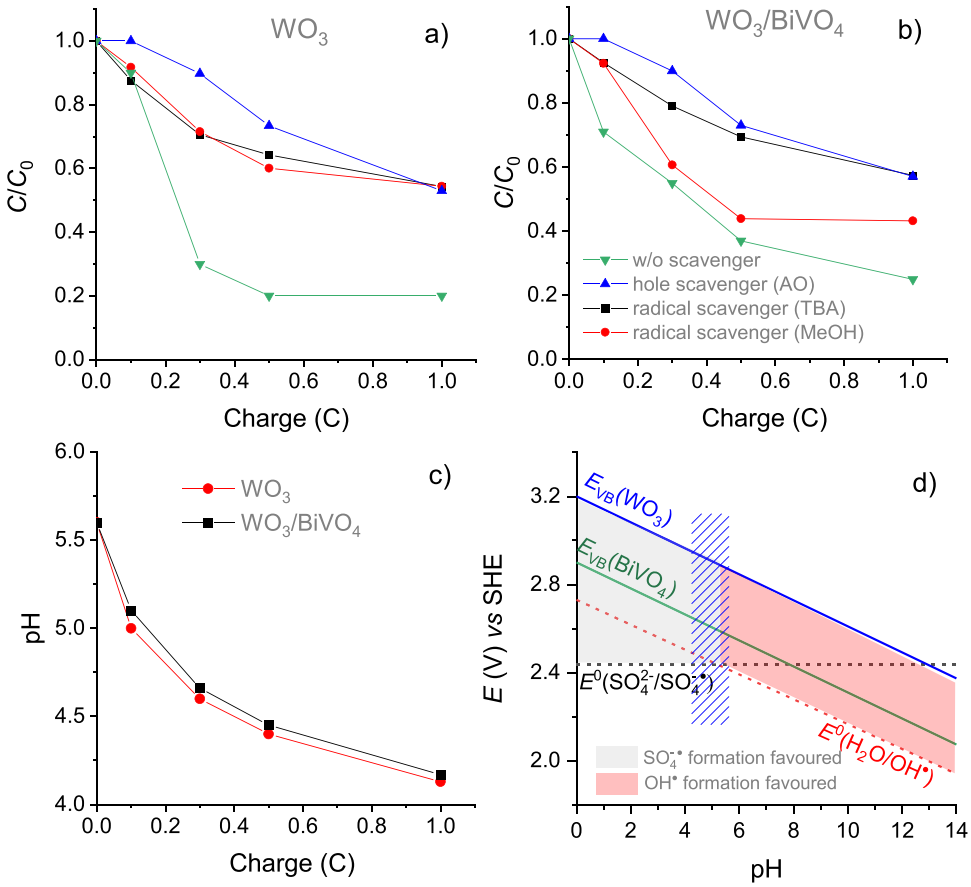

Figure 5. Progression of DCF degradation as a function of charge consumed in the photoelectrolysis of 0.1 M Na_2SO_4 + 50 mg L^{-1} DFC solution containing 2 mM of AO, TBA, or MeOH as h^+, $HO^•$, or $SO_4^{-•}$ scavengers, respectively, using (a) WO_3 or (b) $WO_3/BiVO_4$ photoelectrode. (c) Variation of electrolyte pH during photoelectrolysis. (d) pH dependence of the energy levels of h^+ in WO_3 and $BiVO_4$ as well as $H_2O/HO^•$ and $SO_4^{2-}/SO_4^{-•}$ redox couples; gray and pink shaded areas represent the pH ranges where, respectively, the formation of either $SO_4^{-•}$ or $HO^•$ by photoinduced holes is thermodynamically favored; blue patterned area shows the working pH range.

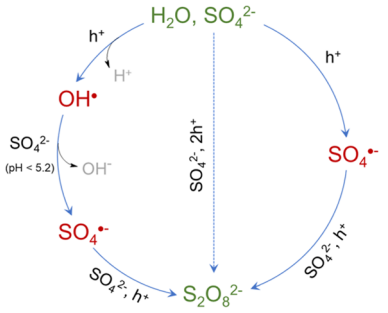

Figure 6. Mechanisms of persulfate ion formation in photoelectrochemical systems involving radical and nonradical pathways.

within the first hour of photoelectrolysis declined by no more than 10% during the next 5−6 h in longer experiments. Another notable feature is that in each consecutive photoelectrolysis experiment, the photocurrent consistently started at nearly the same value as in the previous run, indicating partial regeneration of the photoelectrode surface. It is worth noting that a slight decrease in the pH of the electrolyte during photoelectrolysis (Figure 5c) is beneficial to the stability of WO_3, as this semiconductor is intrinsically unstable at pH > 4.[66,67] This was further corroborated by comparative stability tests in DCF-containing unbuffered and borate-buffered (pH 8.5) 0.1 M Na_2SO_4 electrolytes. A series of consecutively recorded chronoamperograms corresponding to the passage of 0.1, 0.3, 0.5, and 1 C of charge (Figure 7a−d) demonstrate stable photocurrents in all cases except for WO_3 in borate-buffered solution with pH = 8.5. After ∼2500 s, the photocurrent started to decline, and the dissolution of the photoactive layer could be visually observed, as shown in the photos of the photoelectrodes taken before and after the experiment (Figure S7). These results indicate that heterostructuring with $BiVO_4$ can be an effective strategy to protect WO_3 from photocorrosion in solutions with pH > 4.

4. CONCLUSIONS

In this study, an advanced oxidation process based on the photoelectrochemical in situ generation of persulfate using WO_3 and $WO_3/BiVO_4$ photoanodes in a simple aqueous sulfate solution under visible light illumination was demonstrated. The Faradaic efficiencies of light-induced generation of $S_2O_8^{2-}$ were as high as 84 and 71% for WO_3 and $WO_3/BiVO_4$, respectively. The decomposition of diclofenac, amoxicillin, and tetracycline was investigated, and the highest degradation efficiency of ∼80% was found for DCF. The degradation of antibiotics (AMX and TTC) occurred at a much lower rate, with efficiencies of 10−14 and 19−21%, respectively. The mechanism of light-induced degradation of DCF was investigated by comparing the results obtained under photoelectrochemical, photocatalytic, electrochemical, and chemical

https://doi.org/10.1021/acsomega.4c10891
ACS Omega 2025, 10, 8538−8550

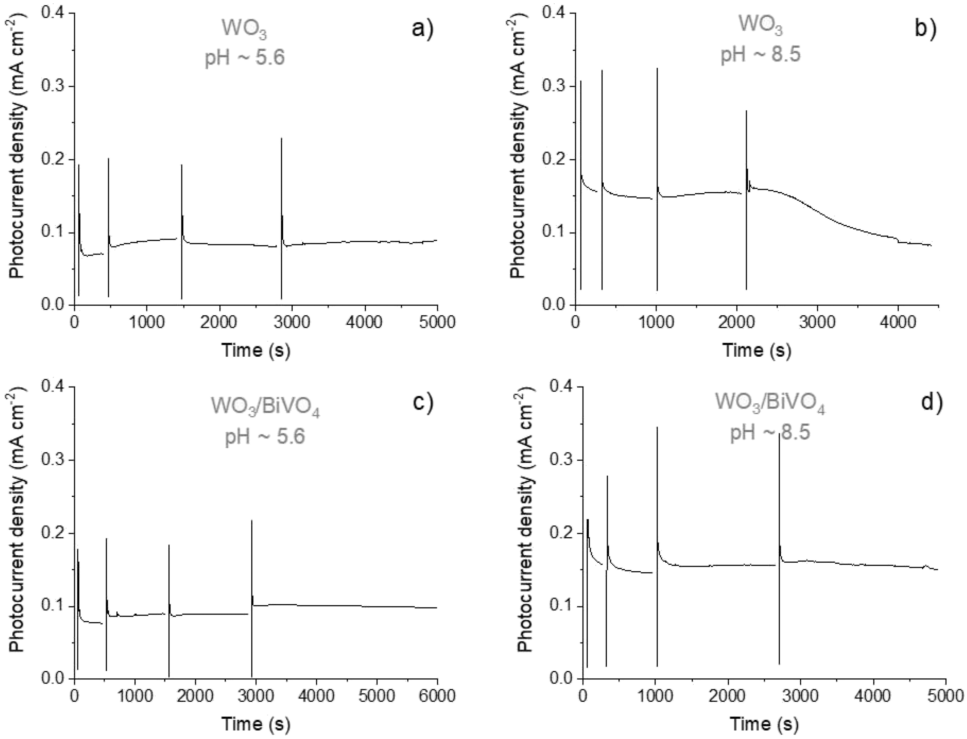

Figure 7. Chronoamperograms of WO_3 (a, b) and $WO_3/BiVO_4$ (c, d) photoelectrodes recorded in unbuffered (a, c) and borate-buffered (pH = 8.5) (b, d) 0.1 M Na_2SO_4 electrolyte containing 50 mg L^{-1} of DCF at an applied bias of 1.4 V (a, c) and 0.8 V (a, d) (vs Pt).

oxidation treatments. Decomposition of DCF under chemical treatment with $S_2O_8^{2-}$ was found to be more than twice less effective compared to PEC treatment. It was suggested that persulfate in the investigated PEC systems could be generated through either nonradical or radical mechanisms. The involvement of radicals was evidenced by quenching experiments using scavengers. On the basis of the results obtained, direct (eqs i and iv) or $HO^{\bullet}$-mediated (eqs ii–iv) pathways of $S_2O_8^{2-}$ formation were proposed.

$$SO_4^{2-} + h^+ \rightarrow SO_4^{-\bullet}; \quad E^0 = 2.437 \text{ V vs SHE} \tag{i}$$

$$H_2O + h^+ \rightarrow HO^{\bullet} + H^+; \quad E^0 = (2.730 - 0.059\text{pH}) \text{ V vs SHE} \tag{ii}$$

$$HO^{\bullet} + SO_4^{2-} \rightarrow SO_4^{-\bullet} + OH^- \quad \text{(thermodynamically possible at pH} < 5.2) \tag{iii}$$

$$SO_4^{-\bullet} + SO_4^{2-} + h^+ \rightarrow S_2O_8^{2-}; \quad E^0 = 1.44 \text{ V vs SHE} \tag{iv}$$

The pH of the 0.1 M Na_2SO_4 solution during photoelectrolysis was found to decrease from 5.6 to 4.2 for both photoanodes, implying that both radical-mediated routes are possible because of the proximity of potentials of $HO^{\bullet}$ and $SO_4^{-\bullet}$ formation under the experimental conditions of this study.

The formation of the $WO_3/BiVO_4$ heterojunction was found to improve the charge carrier separation. However, pure WO_3 demonstrated greater effectiveness in the photoelectrochemical degradation of pharmaceutical compounds. This superior performance was attributed to the higher oxidizing potential of photogenerated holes in WO_3, highlighting that the intrinsic properties of the semiconductor in direct contact with the electrolyte play a crucial role in determining the efficiency of the PEC degradation processes. On the other hand, the deposition of a $BiVO_4$ overlayer was shown to mitigate the intrinsic instability of WO_3 in solutions with pH > 4. The results highlight the importance of the PEC–AOS system optimization to maximize the degradation efficiency of pharmaceuticals.

■ ASSOCIATED CONTENT

Supporting Information

The Supporting Information is available free of charge at https://pubs.acs.org/doi/10.1021/acsomega.4c10891.

Schematics of the photoelectrolysis cell (Figure S1); EDX spectra and cross-sectional SEM images of WO_3 and $WO_3/BiVO_4$ samples (Figure S2); high-resolution XPS spectra of WO_3 and $WO_3/BiVO_4$ surfaces (Figure S3); results of the evolution of the decomposition of pharmaceuticals over time in a 0.1 M Na_2SO_4 electrolyte that has been subjected to photoelectrolysis (Figure S4); variation of C/C_0 of pharmaceuticals under photoelectrochemical, electrochemical, photocatalytic, and chemical oxidative treatments in 0.1 M Na_2SO_4 (Figure S6); and photos of WO_3 and $WO_3/BiVO_4$ photoelectrodes before and after photoelectrolysis in unbuffered and then borate-buffered sulfate electrolytes containing DCF (PDF)

■ AUTHOR INFORMATION

Corresponding Author

Arunas Ramanavicius – *Department of Physical Chemistry, Institute of Chemistry, Faculty of Chemistry and Geosciences, Vilnius University, LT-03225 Vilnius, Lithuania; Department of Nanotechnology, Centre for Physical Sciences*

https://doi.org/10.1021/acsomega.4c10891
ACS Omega 2025, 10, 8538–8550

and Technology, LT-10257 Vilnius, Lithuania; orcid.org/0000-0002-0885-3556; Email: arunas.ramanavicius@chf.vu.lt

Authors

Milda Petruleviciene − *Department of Chemical Engineering and Technology, Centre for Physical Sciences and Technology, LT-10257 Vilnius, Lithuania*

Irena Savickaja − *Department of Chemical Engineering and Technology, Centre for Physical Sciences and Technology, LT-10257 Vilnius, Lithuania*

Jelena Kovger-Jarosevic − *Department of Chemical Engineering and Technology, Centre for Physical Sciences and Technology, LT-10257 Vilnius, Lithuania*

Jurga Juodkazyte − *Department of Chemical Engineering and Technology, Centre for Physical Sciences and Technology, LT-10257 Vilnius, Lithuania*

Audrius Padarauskas − *Department of Analytical and Environmental Chemistry, Institute of Chemistry, Faculty of Chemistry and Geosciences, Vilnius University, LT-03225 Vilnius, Lithuania*

Asta Griguceviciene − *Department of Chemical Engineering and Technology, Centre for Physical Sciences and Technology, LT-10257 Vilnius, Lithuania*

Complete contact information is available at: https://pubs.acs.org/10.1021/acsomega.4c10891

Author Contributions

M.P.: formal analysis, writing—original draft, visualization, and investigation. I.S., J.K.-J., and A.G.: formal analysis. J.J.: conceptualization, visualization, and writing—review and editing. A.P.: formal analysis and visualization. A.R.: supervision and writing—review and editing.

Notes

The authors declare no competing financial interest.

■ ACKNOWLEDGMENTS

This research was funded from a postdoctoral fellowship project, No. S-PD-22-2, funded by the Research Council of Lithuania (LMTLT).

■ ABBREVIATIONS

ABPE, applied bias photon-to-current efficiency; AMX, amoxicillin; AO, ammonium oxalate; AOP, advanced oxidation process; AOS, advanced oxidation systems; CA, chronoamperometry, chronoamperogram; CV, cyclic voltammetry, cyclic voltammogram; DCF, diclofenac; EDX, energy-dispersive X-ray analysis; EIS, electrochemical impedance spectroscopy; FE, Faradaic efficiency; GIXRD, grazing incidence X-ray diffraction; MeOH, methanol; PEG, poly(ethylene glycol); PEC−AOS, photoelectrochemical advanced oxidation system; RSS, reactive sulfate species; SEM, scanning electron microscopy; SHE, standard hydrogen electrode; TBA, *tert*-butyl alcohol; TCC, tetracycline; XRD, X-ray diffraction

■ REFERENCES

(1) Morin-Crini, N.; Lichtfouse, E.; Fourmentin, M.; Ribeiro, A. R. L.; Noutsopoulos, C.; Mapelli, F.; Fenyvesi, É.; Vieira, M. G. A.; Picos-Corrales, L. A.; Moreno-Piraján, J. C.; Giraldo, L.; Sohajda, T.; Huq, M. M.; Soltan, J.; Torri, G.; Magureanu, M.; Bradu, C.; Crini, G. Removal of Emerging Contaminants from Wastewater Using Advanced Treatments. A Review. *Environ. Chem. Lett.* 2022; Vol.*20*, pp1333−1375.

(2) Phoon, B. L.; Ong, C. C.; Mohamed Saheed, M. S.; Show, P. L.; Chang, J. S.; Ling, T. C.; Lam, S. S.; Juan, J. C. Conventional and Emerging Technologies for Removal of Antibiotics from Wastewater. *J. Hazard. Mater.* **2020**, *400*, No. 122961.

(3) Eniola, J. O.; Kumar, R.; Barakat, M. A.; Rashid, J. A Review on Conventional and Advanced Hybrid Technologies for Pharmaceutical Wastewater Treatment. *J. Cleaner Prod.* **2022**, *356*, No. 131826.

(4) Reis, R. Y. N.; Goulart, L. A.; Mascaro, L. H.; Alves, S. A. A Critical View of the Contributions of Photoelectrochemical Technology to Pharmaceutical Degradation. *J. Environ. Chem. Eng.* **2022**, *10* (3), No. 107859.

(5) Lee, J.; Von Gunten, U.; Kim, J. H. Persulfate-Based Advanced Oxidation: Critical Assessment of Opportunities and Roadblocks. *Environ. Sci. Technol.* **2020**, *54* (6), 3064−3081.

(6) Orimolade, B. O.; Arotiba, O. A. Bismuth Vanadate in Photoelectrocatalytic Water Treatment Systems for the Degradation of Organics: A Review on Recent Trends. *J. Electroanal. Chem.* **2020**, *878*, No. 114724.

(7) Koiki, B. A.; Muzenda, C.; Jayeola, K. D.; Zhou, M.; Marken, F.; Arotiba, O. A. Sulfate Radical in (Photo)Electrochemical Advanced Oxidation Processes for Water Treatment: A Versatile Approach. *J. Phys. Chem. Lett.* **2023**, *14* (39), 8880−8889.

(8) Koiki, B. A.; Orimolade, B. O.; Zwane, B. N.; Nkwachukwu, O. V.; Muzenda, C.; Ojo, B. O.; Nkosi, D.; Mabuba, N.; Arotiba, O. A. Sulphate Radical Enhanced Photoelectrochemical Degradation of Sulfamethoxazole on a Fluorine Doped Tin Oxide - Copper(I) Oxide Photoanode. *J. Electroanal. Chem.* **2021**, *900*, No. 115714.

(9) Wacławek, S.; Lutze, H. V.; Grübel, K.; Padil, V. V. T.; Černík, M.; Dionysiou, D. D. Chemistry of Persulfates in Water and Wastewater Treatment: A Review. *Chem. Eng. J.* **2017**, *330*, 44−62.

(10) Liu, Y.; Zhang, Y.; Guo, H.; Cheng, X.; Liu, H.; Tang, W. Persulfate-Assisted Photodegradation of Diethylstilbestrol Using Monoclinic BiVO4 under Visible-Light Irradiation. *Environ. Sci. Pollut. Res.* **2017**, *24* (4), 3739−3747.

(11) Cao, V. D.; Nong, L. X.; Nguyen, V. H.; Tran, T. V.; Vu, H. T.; Nguyen, C. V.; Do, S. T. High Degradation of BIVO4 Nanoparticle for Organic Dyes under Visible Light Irradiation Mediated by S_2O_8. *IOP Conf. Ser. Mater. Sci. Eng.* **2020**, *736* (4), No. 042019.

(12) Murgolo, S.; De Ceglie, C.; Di Iaconi, C.; Mascolo, G. Novel TiO_2-Based Catalysts Employed in Photocatalysis and Photoelectrocatalysis for Effective Degradation of Pharmaceuticals (PhACs) in Water: A Short Review. *Curr. Opin. Green Sustainable Chem.* **2021**, *30*, No. 100473.

(13) Torres-Pinto, A.; Díez, A. M.; Silva, C. G.; Faria, J. L.; Sanromán, M. Á.; Silva, A. M. T.; Pazos, M. Photoelectrocatalytic Degradation of Pharmaceuticals Promoted by a Metal-Free G-C_3N_4 Catalyst. *Chem. Eng. J.* **2023**, *476*, No. 146761, DOI: 10.1016/j.cej.2023.146761.

(14) Petruleviciene, M.; Parvin, M.; Savickaja, I.; Gece, G.; Naujokaitis, A.; Pakstas, V.; Pilipavicius, J.; Gegeckas, A.; Gaigalas, G.; Juodkazyte, J. WO_3 Coatings for Photoelectrochemical Synthesis of Persulfate: Efficiency, Stability and Applicability. *J. Solid State Electrochem.* **2022**, *26* (4), 1021−1035.

(15) Sayama, K. Production of High-Value-Added Chemicals on Oxide Semiconductor Photoanodes under Visible Light for Solar Chemical-Conversion Processes. *ACS Energy Lett.* **2018**, *3* (5), 1093−1101.

(16) Liu, X.; Gu, S.; Zhao, Y.; Zhou, G.; Li, W. BiVO4, Bi2WO6 and Bi2MoO6 Photocatalysis: A Brief Review. *J. Mater. Sci. Technol.* **2020**, *56*, 45−68.

(17) Murillo-Sierra, J. C.; Hernández-Ramírez, A.; Hinojosa-Reyes, L.; Guzmán-Mar, J. L. A Review on the Development of Visible Light-Responsive WO_3-Based Photocatalysts for Environmental Applications. *Chem. Eng. J. Adv.* **2021**, *5*, No. 100070, DOI: 10.1016/j.ceja.2020.100070.

(18) Petruleviciene, M.; Juodkazyte, J.; Parvin, M.; Tereshchenko, A.; Ramanavicius, S.; Karpicz, R.; Samukaite-Bubniene, U.; Ramanavicius, A. Tuning the Photo-Luminescence Properties of

Wo3 Layers by the Adjustment of Layer Formation Conditions. *Materials* **2020**, *13* (12), No. 2814.
(19) Speldrich, S.; Wark, M.; Wittstock, G. Metal Oxide Protection Layers for Enhanced Stability and Activity of WO3 Photoanodes in Alkaline Media. *ACS Appl. Energy Mater.* **2023**, *6* (18), 9602−9614.
(20) Ta, C. X. M.; Furusho, Y.; Amano, F. Photoelectrochemical Stability of WO_3/Mo-Doped $BiVO_4$ Heterojunctions on Different Conductive Substrates in Acidic and Neutral Media. *Appl. Surf. Sci.* **2021**, *548*, No. 149251.
(21) Liu, J.; Li, B.; Kong, L.; Xiao, Q.; Huang, S. Surfactants-Assisted Morphological Regulation of BiVO4 Nanostructures for Photocatalytic Degradation of Organic Pollutants in Wastewater. *J. Phys. Chem. Solids* **2023**, *172*, No. 111079, DOI: 10.1016/j.jpcs.2022.111079.
(22) Nguyen, T. D.; Nguyen, V. H.; Nanda, S.; Vo, D. V. N.; Nguyen, V. H.; Van Tran, T.; Nong, L. X.; Nguyen, T. T.; Bach, L. G.; Abdullah, B.; Hong, S. S.; Van Nguyen, T. BiVO4 Photocatalysis Design and Applications to Oxygen Production and Degradation of Organic Compounds: A Review. *Environ. Chem. Lett.* **2020**, *18* (6), 1779−1801.
(23) Ramanavičius, S.; Petrulevičiene, M.; Juodkazyte, J.; Grigucevičiene, A.; Ramanavičius, A. Selectivity of Tungsten Oxide Synthesized by Sol-Gel Method towards Some Volatile Organic Compounds and Gaseous Materials in a Broad Range of Temperatures. *Materials* **2020**, *13* (3), No. 523.
(24) Wang, C.; Zhao, Y.; Cheng, C.; Li, Q.; Guo, C.; Hu, Y. S-Scheme Heterojunction Photocatalysts: Mechanism, Challenges and Opportunities. *Coord. Chem. Rev.* **2024**, *521*, No. 216177.
(25) Su, J.; Guo, L.; Bao, N.; Grimes, C. A. Nanostructured WO_3/$BiVO_4$ Heterojunction Films for Efficient Photoelectrochemical Water Splitting. *Nano Lett.* **2011**, *11* (5), 1928−1933.
(26) Cheng, C.; Xu, H.; Ni, M.; Guo, C.; Zhao, Y.; Hu, Y. Interfacial Electron Interactions Governed Photoactivity and Selectivity Evolution of Carbon Dioxide Photoreduction with Spinel Cobalt Oxide Based Hollow Hetero-Nanocubes. *Appl. Catal., B* **2024**, *345*, No. 123705.
(27) Orimolade, B. O.; Arotiba, O. A. Enhanced Photoelectrocatalytic Degradation of Diclofenac Sodium Using a System of Ag-$BiVO_4$/BiOI Anode and Ag-BiOI Cathode. *Sci. Rep.* **2022**, *12* (1), No. 4214.
(28) Sun, J.; Guo, Y.; Wang, Y.; Cao, D.; Tian, S.; Xiao, K.; Mao, R.; Zhao, X. H2O2 Assisted Photoelectrocatalytic Degradation of Diclofenac Sodium at G-C_3N_4/$BiVO_4$ Photoanode under Visible Light Irradiation. *Chem. Eng. J.* **2018**, *332*, 312−320.
(29) Hua, Z.; Dai, Z.; Bai, X.; Ye, Z.; Wang, P.; Gu, H.; Huang, X. Copper Nanoparticles Sensitized TiO_2 Nanotube Arrays Electrode with Enhanced Photoelectrocatalytic Activity for Diclofenac Degradation. *Chem. Eng. J.* **2016**, *283*, 514−523.
(30) Omrani, N.; Nezamzadeh-Ejhieh, A. A Comprehensive Study on the Mechanism Pathways and Scavenging Agents in the Photocatalytic Activity of $BiVO_4$/WO_3 Nano-Composite. *J. Water Process Eng.* **2020**, *33*, No. 101094.
(31) Chi, Z.; Zhao, J.; Zhang, Y.; Yu, H.; Yu, H. Coral-like WO_3/$BiVO_4$ Photoanode Constructed via Morphology and Facet Engineering for Antibiotic Wastewater Detoxification and Hydrogen Recovery. *Chem. Eng. J.* **2022**, *428*, No. 131817.
(32) Du, H.; Pu, W.; Wang, Y.; Yan, K.; Feng, J.; Zhang, J.; Yang, C.; Gong, J. Synthesis of $BiVO_4$/WO_3 Composite Film for Highly Efficient Visible Light Induced Photoelectrocatalytic Oxidation of Norfloxacin. *J. Alloys Compd.* **2019**, *787*, 284−294.
(33) Davies, K. R.; Allan, M. G.; Nagarajan, S.; Townsend, R.; Dunlop, T.; McGettrick, J. D.; Asokan, V. S.; Ananthraj, S.; Watson, T.; Godfrey, A. R.; Durrant, J. R.; Maroto-Valer, M. M.; Kuehnel, M. F.; Pitchaimuthu, S. Solar Light-Driven Simultaneous Pharmaceutical Pollutant Degradation and Green Hydrogen Production Using a Mesoporous Nanoscale WO3/BiVO4 Heterostructure Photoanode. *J. Environ. Chem. Eng.* **2023**, *11* (3), No. 110256.
(34) Peleyeju, M. G.; Viljoen, E. L. WO_3-Based Catalysts for Photocatalytic and Photoelectrocatalytic Removal of Organic Pollutants from Water − A Review. *J. Water Process Eng.* **2021**, *40*, No. 101930.
(35) Zeng, Q.; Lyu, L.; Gao, Y.; Chang, S.; Hu, C. A Self-Sustaining Monolithic Photoelectrocatalytic/Photovoltaic System Based on a WO_3/$BiVO_4$ Photoanode and Si PVC for Efficiently Producing Clean Energy from Refractory Organics Degradation. *Appl. Catal., B* **2018**, *238*, 309−317.
(36) Petruleviciene, M.; Turuta, K.; Savickaja, I.; Juodkazyte, J.; Ramanavicius, A. Photoelectrochemical Degradation of Organic Compounds via Formed Reactive Chlorine and Sulfate Species by WO_3-Based Photoanodes. *J. Electroanal. Chem.* **2023**, *951*, No. 117954.
(37) Malefane, M. E.; Feleni, U.; Kuvarega, A. T. Cobalt (II/III) Oxide and Tungsten (VI) Oxide p-n Heterojunction Photocatalyst for Photodegradation of Diclofenac Sodium under Visible Light. *J. Environ. Chem. Eng.* **2020**, *8* (2), No. 103560.
(38) Pobozy, E.; Kaczmarek, S.; Miecznikowski, K.; Pyrzynska, K.; Biesaga, M. Photocatalytic Degradation of Selected Non-Opioid Analgesics Driven by Solar Light Exposure. *Appl. Sci.* **2024**, *14* (17), No. 7768.
(39) Mugunthan, E.; Saidutta, M. B.; Jagadeeshbabu, P. E. Photocatalytic Activity of ZnO-WO_3 for Diclofenac Degradation under Visible Light Irradiation. *J. Photochem. Photobiol., A* **2019**, *383*, No. 111993.
(40) Cheng, X.; Wang, P.; Liu, H. Visible-Light-Driven Photoelectrocatalytic Degradation of Diclofenac by N, S-TiO_2/TiO_2 NTs Photoelectrode: Performance and Mechanism Study. *J. Environ. Chem. Eng.* **2015**, *3* (3), 1713−1719.
(41) Cheng, X.; Liu, H.; Chen, Q.; Li, J.; Wang, P. Enhanced Photoelectrocatalytic Performance for Degradation of Diclofenac and Mechanism with TiO2 Nano-Particles Decorated TiO_2 Nano-Tubes Arrays Photoelectrode. *Electrochim. Acta* **2013**, *108*, 203−210.
(42) G, B.; Banat, F.; Abu Haija, M. Photoelectrochemical Advanced Oxidation Processes for Simultaneous Removal of Antibiotics and Heavy Metal Ions in Wastewater Using 2D-on-2D WS_2@$CoFe_2O_4$ Heteronanostructures. *Environ. Pollut.* **2023**, *339*, No. 122753.
(43) Haddadou, N.; Bensemma, N.; Rekhila, G.; Trari, M.; Taïbi, K. Photoelectrochemical Properties of the Relaxor $Ba(Ti_{0.90}Sc_{0.05}Nb_{0.05})O_3$: Application to the Degradation of Amoxicillin under Solar Light. *J. Mater. Sci.: Mater. Electron.* **2018**, *29* (6), 5042−5048.
(44) Wang, J.; Jiang, L.; Liu, F.; Jia, M.; Liu, M.; Li, J.; Lai, Y. Enhanced Photoelectrochemical Degradation of Tetracycline Hydrochloride with FeOOH and Au Nanoparticles Decorated WO_3. *Chem. Eng. J.* **2021**, *407*, No. 127195.
(45) Le, H. V.; Le, L. T.; Han, H.; Ung, T. T. D.; Tran, P. D. Photoelectrodeposition of Ag_3PO_4 Nanoparticles on $BiVO_4$ Photoanode for Enhancing Its Photoelectrochemical Water Oxidation Performance. *J. Sci. Adv. Mater. Devices* **2023**, *8* (2), No. 100547.
(46) Chen, Z.; N Dinh, H.; Miller, E. *Photoelectrochemical Water Splitting Standards, Experimental Methods, and Protocols*; Springer: New York, NY, 2013.
(47) Armstrong, D. A.; Huie, R. E.; Koppenol, W. H.; Lymar, S. V.; Merenyi, G.; Neta, P.; Ruscic, B.; Stanbury, D. M.; Steenken, S.; Wardman, P. Standard Electrode Potentials Involving Radicals in Aqueous Solution: Inorganic Radicals (IUPAC Technical Report). *Pure Appl. Chem.* **2015**, *87* (11−12), 1139−1150.
(48) Parvin, M.; Petrulevičienė, M.; Savickaja, I.; Šebeka, B.; Karpicz, R.; Grigucevičienė, A.; Ramanauskas, R.; Juodkazytė, J. Influence of Morphology on Photoanodic Behaviour of WO_3 Films in Chloride and Sulphate Electrolytes. *Electrochim. Acta* **2022**, *403*, No. 139710.
(49) Szilágyi, I. M.; Janos, M.; Pokol, G.; Kiraly, P.; Gabor, T.; Sami, S.; Janos, M.; Attila, T.; Andras, S.; Katalin, V.-J. Stability and Controlled Composition of Hexagonal WO_3. *Chem. Mater.* **2008**, *20* (12), 4116−4125.
(50) Wei, P.; Wen, Y.; Lin, K.; Li, X. 2D/3D WO_3/$BiVO_4$ Heterostructures for Efficient Photoelectrocatalytic Water Splitting. *Int. J. Hydrogen Energy* **2021**, *46* (54), 27506−27515.
(51) Gutkowski, R.; Khare, C.; Conzuelo, F.; Kayran, Y. U.; Ludwig, A.; Schuhmann, W. Unraveling Compositional Effects on the Light-

Induced Oxygen Evolution in Bi(V-Mo-X)O4Material Libraries. *Energy Environ. Sci.* **2017**, *10* (5), 1213−1221.
(52) Wu, J. M.; Chen, Y.; Pan, L.; Wang, P.; Cui, Y.; Kong, D. C.; Wang, L.; Zhang, X.; Zou, J. J. Multi-Layer Monoclinic $BiVO_4$ with Oxygen Vacancies and V^{4+} Species for Highly Efficient Visible-Light Photoelectrochemical Applications. *Appl. Catal., B* **2018**, *221*, 187−195.
(53) Shi, X.; Wu, Q.; Cui, C. Modulating WO_3 Crystal Orientation to Suppress Hydroxyl Radicals for Sustainable Solar Water Oxidation. *ACS Catal.* **2023**, *13* (2), 1470−1476.
(54) Cristino, V.; Pasti, L.; Marchetti, N.; Berardi, S.; Bignozzi, C. A.; Molinari, A.; Passabi, F.; Caramori, S.; Amidani, L.; Orlandi, M.; Bazzanella, N.; Piccioni, A.; Kopula Kesavan, J.; Boscherini, F.; Pasquini, L. Photoelectrocatalytic Degradation of Emerging Contaminants at $WO_3/BiVO_4$ Photoanodes in Aqueous Solution. *Photochem. Photobiol. Sci.* **2019**, *18* (9), 2150−2163.
(55) Wang, J.; Wang, S. Reactive Species in Advanced Oxidation Processes: Formation, Identification and Reaction Mechanism. *Chem. Eng. J.* **2020**, *401*, No. 126158.
(56) Kumari, M.; Pulimi, M. Sulfate Radical-Based Degradation of Organic Pollutants: A Review on Application of Metal-Organic Frameworks as Catalysts. *ACS Omega* **2023**, *8* (38), 34262−34280.
(57) Monfort, O.; Plesch, G. Bismuth Vanadate-Based Semiconductor Photocatalysts: A Short Critical Review on the Efficiency and the Mechanism of Photodegradation of Organic Pollutants. *Environ. Sci. Pollut. Res.* **2018**, *25* (20), 19362−19379.
(58) Sun, B.; Li, H.; Wei, Q.; Xue, S.; Zhou, A.; Yue, X. Enhanced Quinoline Degradation by Persulfate-Assisted Photocatalytic Process with WO_3-$CuFe_2O_4$ Z-Scheme System: Properties and Mechanism. *Sep. Purif. Technol.* **2022**, *301*, No. 122039.
(59) Ambrosio, F.; Wiktor, J.; Pasquarello, A. PH-Dependent Catalytic Reaction Pathway for Water Splitting at the $BiVO_4$-Water Interface from the Band Alignment. *ACS Energy Lett.* **2018**, *3* (4), 829−834.
(60) Chen, S.; Wang, L. W. Thermodynamic Oxidation and Reduction Potentials of Photocatalytic Semiconductors in Aqueous Solution. *Chem. Mater.* **2012**, *24* (18), 3659−3666.
(61) Bacha, A. U. R.; Nabi, I.; Cheng, H.; Li, K.; Ajmal, S.; Wang, T.; Zhang, L. Photoelectrocatalytic Degradation of Endocrine-Disruptor Bisphenol − A with Significantly Activated Peroxymonosulfate by Co-$BiVO_4$ Photoanode. *Chem. Eng. J.* **2020**, *389*, No. 124482.
(62) Wang, L.; Liu, Z.; Xu, X.; Jia, Y.; Mei, Q.; Ding, F.; Peng, J.; Wang, Q. Efficient Solar Water Splitting via Enhanced Charge Separation of the $BiVO_4$ Photoanode. *ACS Appl. Energy Mater.* **2022**, *5* (5), 6383−6392.
(63) Nasseri, S.; Mahvi, A. H.; Seyedsalehi, M.; Yaghmaeian, K.; Nabizadeh, R.; Alimohammadi, M.; Safari, G. H. Degradation Kinetics of Tetracycline in Aqueous Solutions Using Peroxydisulfate Activated by Ultrasound Irradiation: Effect of Radical Scavenger and Water Matrix. *J. Mol. Liq.* **2017**, *241*, 704−714.
(64) Paquin, F.; Rivnay, J.; Salleo, A.; Stingelin, N.; Silva, C. Multi-Phase Semicrystalline Microstructures Drive Exciton Dissociation in Neat Plastic Semiconductors. *J. Mater. Chem. C* **2015**, *3*, 10715−10722.
(65) Liang, C.; Su, H. W. Identification of Sulfate and Hydroxyl Radicals in Thermally Activated Persulfate. *Ind. Eng. Chem. Res.* **2009**, *48* (11), 5558−5562.
(66) Anik, M. PH-Dependent Anodic Reaction Behavior of Tungsten in Acidic Phosphate Solutions. *Electrochim. Acta* **2009**, *54* (15), 3943−3951.
(67) Nave, M. I.; Kornev, K. G. Complexity of Products of Tungsten Corrosion: Comparison of the 3D Pourbaix Diagrams with the Experimental Data. *Metall. Mater. Trans. A* **2017**, *48* (3), 1414−1424.

https://doi.org/10.1021/acsomega.4c10891
ACS Omega 2025, 10, 8538−8550